

Deterministic Neural SDEs for Affordable Uncertainty Quantification

Andreas Look¹ Melih Kandemir¹ Jan Peters²

Abstract

Neural Stochastic Differential Equations (NSDEs) model the drift and diffusion functions of a stochastic process as neural networks. While NSDEs are known to predict time series accurately, their uncertainty quantification properties remain unexplored. We report the empirical finding that obtaining well-calibrated uncertainty estimations from NSDEs is computationally prohibitive. As a remedy, we develop a computationally affordable deterministic scheme for expressing the likelihood of a sequence, when dynamics is governed by a NSDE, which is applicable to both training and prediction. Our method introduces a bidirectional moment matching scheme, one vertical along the neural net layers, and one horizontal along the time direction, which benefits from an original combination of effective approximations. We observe in multiple experiments that the uncertainty calibration quality of our method can be matched by Monte Carlo sampling only after introducing at least five times more computation cost. Thanks to the numerical stability of deterministic training, our method also provides improvement in prediction accuracy.

1. Introduction

Accompanying time series predictions with calibrated uncertainty scores is a challenging problem. The main difficulty is that uncertainty assessments for individual time points propagate, causing local errors to impair the predictions on the whole sequence. While calibrated prediction is well-studied for feed-forward neural networks (Platt, 1999; Thiagarajan et al., 2020), the same problem is a relatively new challenge for predictors with feedback loops. The few prior work is restricted to post-hoc calibration of deterministic recurrent neural nets (Kuleshov et al., 2018; Cui et al., 2020).

We report the first study on the uncertainty quantification

characteristics of *Neural Stochastic Differential Equations* (NSDEs) (Tzen & Raginsky, 2019; Li et al., 2020). A Neural SDE models the continuous dynamics of an environment with a drift neural net governing the deterministic component of a vector field and a diffusion neural net governing the instantaneous distortions. Neural SDEs have a large potential to provide an attractive tool to the machine learning community due to their strong theoretical links to *Recurrent Neural Nets* (RNNs), *Neural ODEs* (NODEs), and *Gaussian Processes* (GPs) (Särkkä & Solin, 2019; Hegde et al., 2019). While multiple studies have observed NSDEs to bring encouraging success in prediction accuracy, none has thus far investigated their performance in uncertainty quantification. Yet, an essential benefit of modeling stochasticity is to account for uncertainty in a reliable way.

We focus on a central observation: Solving NSDEs with Monte Carlo sampling requires a prohibitively large sample set, i.e. computation time, for accurate uncertainty quantification. We introduce an original method for deterministic prediction with NSDEs that can deliver well-calibrated prediction uncertainties at significantly lower computational cost than Monte Carlo sampling by the virtue of

- i) performing bidirectional moment matching to approximate the intractable expectation and covariance integrals: horizontally across time and vertically across the layers of the drift and diffusion neural nets,
- ii) using Steins’s lemma to simplify calculation of covariances while matching moments across time, and
- iii) approximating the expected Jacobian of a neural net accurately while matching moments across layers.

Differently from the prior art of moment matching in deterministic neural net inference (Wu et al., 2019), the intractable expressions are caused by the randomness of the input instead of the stochasticity of the neural net weights. As visualized for a toy case in Fig. 1, NSDE prediction with Monte Carlo sampling requires a large sample set to catch up with the calibration level of our deterministic method. We observe in three applications that using our method for both training and prediction brings the highest prediction accuracy and the most calibrated uncertainties.

¹Bosch Center for Artificial Intelligence, Renningen, Germany

²Intelligent Autonomous Systems, TU Darmstadt, Germany. Correspondence to: Andreas Look <andreas.look@bosch.com>.

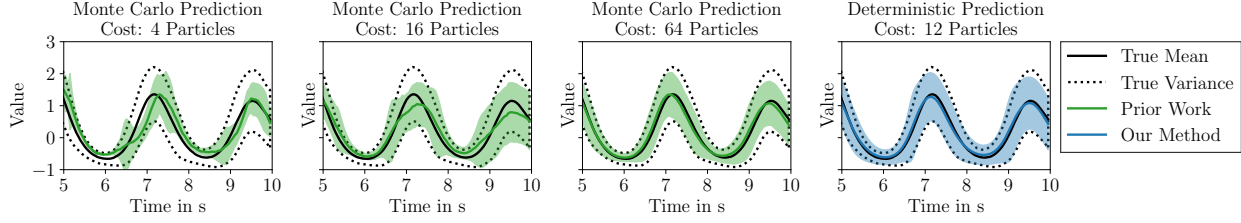


Figure 1. Our deterministic approximation provides well-calibrated uncertainty scores with a computational cost equal to 12 particles. Reaching a comparable level of calibration by Monte Carlo sampling demands at least 64 particles.

2. Neural Stochastic Differential Equations

We are concerned with the model family that describes the dynamics of a D -dimensional stochastic process x_t as a non-linear time-invariant SDE

$$dx_t = f_\theta(x_t)dt + L_\phi(x_t)dw_t. \quad (1)$$

Above, $f_\theta(x_t) : \mathbb{R}^D \rightarrow \mathbb{R}^D$ is the drift function governing the deterministic component of the SDE, which is modeled as a neural net with an arbitrary architecture. Similarly, the diffusion function $L_\phi(x_t) : \mathbb{R}^D \rightarrow \mathbb{R}^{D \times D}$ is another neural net, which models the stochasticity of the system. Further, dt is the time increment and w_t is a D -dimensional standard Wiener process that injects instantaneous noise into the dynamics following a normal distribution with variance proportional to the time increment.

In order to make a prediction at time point T , the below system needs to be solved

$$x_T = x_0 + \int_0^T f_\theta(x_t)dt + \int_0^T L_\phi(x_t)dw_t, \quad (2)$$

where x_0 is the provided initial value. The integral involving the drift function is defined within the classical calculus, though its solution is a random variable. The second integral involving the diffusion is with respect to the Wiener process dw_t , hence defined by the Itô calculus (Oksendal, 1992). The randomness induced at every infinitesimal time step by dw_t makes the solution x_T a random variable that follows a probability distribution $p_{\theta,\phi}(x_T|x_0)$, referred to as a stochastic process parameterized by θ, ϕ .

As the Wiener process injects randomness to any arbitrarily small time interval, solution of any NSDE with drift and diffusion networks with at least one hidden layer is analytically intractable. As a numerical approximation, we adopt the *Euler-Maruyama* (EM) discretization due to its computational efficiency:

$$x_{k+1} := x_k + f_\theta(x_k)\Delta t + L_\phi(x_k)\Delta w_k, \quad (3)$$

where $\Delta w_k \sim \mathcal{N}(0, \Delta t)$. The choice of the time step size $\Delta t > 0$ is arbitrary, and can be chosen dynamically

if desired. For notational clarity, we assume a uniform discretization, which amounts to the below approximation on the stochastic process density

$$p_{\theta,\phi}(x_{k+1}|x_k) \approx p_{\theta,\phi}^{\text{EM}}(x_{k+1}|x_k) \quad (4)$$

$$:= \mathcal{N}(x_{k+1}|m_{k+1}(x_k), S_{k+1}(x_k)),$$

where $m_{k+1}(x_k) := x_k + f_\theta(x_k)\Delta t$ and $S_{k+1}(x_k) := L_\phi(x_k)L_\phi(x_k)^T\Delta t$ are the mean and variance of a normal density.

We may express the joint distribution of a time series $X = \{x_0, \dots, x_K\}$ governed by the SDE in Eq. 1, which is observed on $K+1$ time points, as

$$p_{\theta,\phi}(X) = p(x_0) \prod_{k=0}^{K-1} p_{\theta,\phi}(x_{k+1}|x_k),$$

$$\approx p(x_0) \prod_{k=0}^{K-1} p_{\theta,\phi}^{\text{EM}}(x_{k+1}|x_k), \quad (5)$$

$$= p(x_0) \prod_{k=0}^{K-1} \mathcal{N}(x_{k+1}|m_{k+1}(x_k), S_{k+1}(x_k)),$$

where $p(x_0)$ is assumed to be given or learnable. Above we approximate the intractable factors $p_{\theta,\phi}(x_{k+1}|x_k)$ with the EM discretization introduced in Eq. 4 and use the Markovian structure of the NSDE.

We are interested in fitting θ and ϕ to an observed sample set $\mathcal{D} = \{\tilde{X}_1, \dots, \tilde{X}_N\}$ consisting of N time series of arbitrary lengths and resolutions. Unlike in standard parameter identification tasks, NSDE training involves fitting thousands of free parameters even for modestly wide and deep architectures. Hence, many of the existing techniques in the standard SDE literature are inapplicable (Ryder et al., 2018; Abbati et al., 2019). One suitable option is to define a prior distribution for the learnable target process, and infer the intractable posterior by variational inference (Tzen & Raginsky, 2019; Li et al., 2020). This approach comes with the limitation that the prior process has to share the same diffusion function as the target process. Furthermore, there exist many applications where an informative prior process is not available.

In our work, we limit the discussion to the alternative option of learning θ and ϕ by *Maximum Likelihood Estimation* (MLE), though adaptation of our method to variational inference is straightforward. Specifically, we are concerned with the learning problem below

$$\operatorname{argmax}_{\theta, \phi} \sum_{i=1}^N \log p_{\theta, \phi}(X_i = \tilde{X}_i), \quad (6)$$

where $p_{\theta, \phi}(X_i = \tilde{X}_i)$ stands for the probability mass assigned by the stochastic process on the data points of the observed time series \tilde{X}_i . As we do not have access to the marginal distribution of the process, we are not able to evaluate this likelihood. Hence, we need an approximate solution to the marginal process distribution for an arbitrary time step, which calls for the recursive solution

$$p_{\theta, \phi}^{\text{EM}}(x_{k+1}) := \int p_{\theta, \phi}^{\text{EM}}(x_{k+1}|x_k) p_{\theta, \phi}^{\text{EM}}(x_k) dx_k, \quad (7)$$

for all time steps $k = 0, \dots, K$ with $p_{\theta, \phi}^{\text{EM}}(x_0) := p(x_0)$, which is assumed to be given. Once this recursion is solved for all time steps in increasing order, one can evaluate the density of an observed time series by

$$p_{\theta, \phi}(X = \tilde{X}) \approx p(x_0 := \tilde{x}_0) \prod_{k=1}^K p_{\theta, \phi}^{\text{EM}}(x_k := \tilde{x}_k). \quad (8)$$

Prior work (Tzen & Raginsky, 2019; Look & Kandemir, 2019; Li et al., 2020) commonly evaluates the above intractable density via Monte Carlo methods. After sampling multiple trajectories from the NSDE driven Markov process, as defined in Eq. 5, the dependence on the previous time step x_k in Eq. 7 can be marginalized out. As we find out that sampling noise impairs the predictive calibration (see Fig. 1), our goal is derive a deterministic approximation of the intractable density in Eq. 8.

3. Deterministic Likelihood Evaluation with Bidirectional Moment Matching

We craft our deterministic NSDE prediction method in three steps: (i) approximating the process density at every time point as a normal distribution in Eq. 10, (ii) marginalizing out the Wiener process noise from moment matching update rules in Eqs. 12 and 13, (iii) approximating the intractable terms in the moment calculations in Sec. 3.1, 3.2, and 3.3. We present our resulting algorithm in Sec 3.4 and detail moment propagation through neural net layers in Sec. 3.5.

Spelled out in full detail, Eq. 7 stands for

$$p_{\theta, \phi}^{\text{EM}}(x_{k+1}) := \int \mathcal{N}(x_{k+1} | x_k + f_{\theta}(x_k)\Delta t, L_{\phi}(x_k)L_{\phi}(x_k)^T\Delta t) p_{\theta, \phi}^{\text{EM}}(x_k) dx_k, \quad (9)$$

involving an integral with respect to the marginal distribution $p_{\theta, \phi}^{\text{EM}}(x_k)$ of the previous time step applied on a normally distributed integrand involving neural nets $f_{\theta}(x_k)$ and $L_{\phi}(x_k)$. As this integral is intractable for all non-trivial architectures, we approximate the marginal by a normal distribution

$$p_{\theta, \phi}^{\text{EM}}(x_{k+1}) \approx \mathcal{N}(x_{k+1} | \mu_{k+1}, \Sigma_{k+1}), \quad (10)$$

where $\mu_{k+1} := \mathbb{E}[x_{k+1}]$ and $\Sigma_{k+1} := \text{Cov}[x_{k+1}]$. This approximation simplifies the problem to calculating the first two moments of x_{k+1} . Plugging the assumed density in Eq. 10 into the recursive relation for estimation of $p_{\theta, \phi}^{\text{EM}}(x_{k+1})$, as defined in Eq. 7, amounts to approximating the marginal process distribution at every time point k by matching moments progressively in time direction. We refer to this chain of operations as *Horizontal Moment Matching (HMM)*.

Calculating μ_{k+1} and Σ_{k+1} does not appear to be a simpler problem at the first sight than solving Eq. 9. However, it is possible to obtain a more pleasant expression by reparameterizing $p_{\theta, \phi}^{\text{EM}}(x_{k+1})$ as

$$z_k \sim \mathcal{N}(z_k | 0, I), \quad x_k \sim \mathcal{N}(x_k | \mu_k, \Sigma_k), \quad (11)$$

$$x_{k+1} := x_k + f_{\theta}(x_k)\Delta t + L_{\phi}(x_k)\sqrt{\Delta t}z_k,$$

where I is the identity matrix with the dimensionality appropriate for the context. We arrive at the following alternative view of the first moment of $p_{\theta, \phi}^{\text{EM}}(x_{k+1})$ using the law of the unconscious statistician

$$\mu_{k+1} = \mu_k + \mathbb{E}[f_{\theta}(x_k)]\Delta t. \quad (12)$$

The corresponding covariance reads

$$\begin{aligned} \Sigma_{k+1} = & \Sigma_k + \text{Cov}[f_{\theta}(x_k)]\Delta t^2 + \text{Cov}[f_{\theta}(x_k), x_k]\Delta t \\ & + \text{Cov}[f_{\theta}(x_k), x_k]^T\Delta t + \mathbb{E}[L_{\phi}(x_k)L_{\phi}^T(x_k)]\Delta t, \end{aligned} \quad (13)$$

where $\text{Cov}[f_{\theta}(x_k), x_k]$ denotes the cross-covariance between the random vectors in the arguments. Eq. 13 can be derived by integrating out the Wiener process and rewriting the expression according to the bilinearity of the covariance operator. See Appx. A for further details. Moment matching solutions along similar lines have been developed earlier for SDEs (Särkkä & Sarmavuori, 2013). However, they have not yet been tailored for the specific needs of NSDEs.

3.1. Computing the drift network moments

After applying the HMM scheme introduced above, the terms $\mathbb{E}[f_{\theta}(x_k)]$ and $\text{Cov}[f_{\theta}(x_k)]$ amount to the first two moments of a random variable obtained by propagating $x_k \sim \mathcal{N}(\mu_k, \Sigma_k)$ through the neural net

$$f_{\theta}(x_k) = g_L(g_{L-1}(\dots g_2(g_1(x_k)) \dots)),$$

composed of a chain of L simple functions (layers), typically an alternation of affine transformations and nonlinear activations. Calculating the moments of $f_\theta(x_k)$ is analytically intractable due to the nonlinear activations. We approximate this computation by another round of moment matching, this time by propagating the input noise through the neural net. Denote the feature map at layer l at time step k as $h_k^l := g_l(g_{l-1}(\dots g_2(g_1(x_k)) \dots))$, which is a random variable due to x_k and is related recursively to the feature map of the previous layer as $h_k^l = g_l(h_k^{l-1})$. Denoting $h_k^0 := x_k$, we approximate the distributions on layers recursively as

$$h_k^l = g_l(h_k^{l-1}) \approx \tilde{h}_k^l \sim \mathcal{N}(a_k^l, B_k^l), \quad (14)$$

where $a_k^l := \mathbb{E}[g_l(\tilde{h}_k^{l-1})]$ and $B_k^l := \text{Cov}[g_l(\tilde{h}_k^{l-1})]$. We refer to applying this approximation throughout all neural net layers as *Vertical Moment Matching (VMM)*. We provide output moments a_k^l and B_k^l for different layers in Sec. 3.5.

A similar approach has been applied earlier to *Bayesian Neural Nets* (BNN) for random weights in various contexts such as expectation propagation (Hernandez-Lobato & Adams, 2015; Ghosh et al., 2016), deterministic variational inference (Wu et al., 2019), and evidential deep learning (Haussmann et al., 2020). To our knowledge, there is no earlier study that applies this approach to propagating input uncertainty through a deterministic network, especially in the context of time series prediction. As an outcome of VMM, we get $\mathbb{E}[f_\theta(x_k)] \approx a_k^L$ and $\text{Cov}[f_\theta(x_k)] \approx B_k^L$.

3.2. Computing the diffusion network moments

We assume the diffusion matrix $L_\phi(x_t)$ to be diagonal for computational efficiency, though our method generalizes trivially to a full diffusion covariance. Overloading the notation for the sake of brevity, we denote an L -layer neural net assigned to its diagonal entries as $L_\phi(x_k) := u_L(u_{L-1}(\dots u_2(u_1(x_k)) \dots))$ with feature maps defined recursively as $v_k^l := u_l(v_k^{l-1})$. Following VMM, we pass the moments through the network simply by approximating the random (due to noisy x_k) feature map v_k^l by a normal distribution $\tilde{v}_k^l \sim \mathcal{N}(c_k^l, D_k^l)$ applying the moment matching rules to Eq. 14 literally on c_k^l and D_k^l and get as output

$$\mathbb{E}[L_\phi(x_k)L_\phi^T(x_k)] \approx (D_k^L + (c_k^L)(c_k^L)^T) \odot I := D_k, \quad (15)$$

with \odot denoting the Hadamard product. The second central moment D_k is a diagonal matrix due to the restriction of a vector-valued output of $L_\phi(x_k)$. The diagonal elements are equal to the second moment of each output.

3.3. Computing the cross-covariance

The term $\text{Cov}[f_\theta(x_k), x_k]$ stands for the cross-covariance between the input x_k , which is itself a random variable, and its transformation with the drift function $f_\theta(x_k)$. Due to

the same reasons as the mean and covariance of $f_\theta(x_k)$, this cross-covariance term cannot be analytically calculated except for trivial drift functions. However, cross-covariance is not provided as a direct outcome of VMM. As being neither a symmetric nor a positive semi-definite matrix, inaccurate approximation of cross-covariance may result in a singular Σ_{k+1} and impair numerical stability. This fact provides us yet another motivation for maintaining our method deterministic. Applying Stein's lemma (Liu, 1994)

$$\text{Cov}[x_k, f_\theta(x_k)] = \text{Cov}[x_k, x_k] \mathbb{E}[\nabla_{x_k} f_\theta(x_k)] \quad (16)$$

for the first time in the context of matching moments of a neural net, we obtain a form that is easier to approximate. The covariance $\text{Cov}[x_k, x_k]$ is provided from the previous time step as Σ_k , but the expected gradient $\mathbb{E}[\nabla_{x_k} f_\theta(x_k)]$ needs to be explicitly calculated. In standard BNN inference, where the source of uncertainty is the weights, we have the interchangeability property for the gradients with respect to the weight distribution parameters ξ as $\nabla_\xi \mathbb{E}_{q(\theta|\xi)}[f_\theta(x_k)] = \mathbb{E}_{q(\theta|\xi)}[\nabla_\xi f_\theta(x_k)]$. This trick is not applicable to our case as the gradient is with respect to x . In other words, $\mathbb{E}[\nabla_{x_k} f_\theta(x_k)]$ is not equal to $\nabla_{x_k} \mathbb{E}[f_\theta(x_k)]$, which would otherwise allow us to simply use $\nabla \mu_k$.

We define the Jacobian matrix of the output of a vector-variate function g with respect to its input x as $\nabla_x g(x)$. Applying the chain rule, the expectation of the derivative of a neural net with respect to a random input reads

$$\mathbb{E}[\nabla_{x_k} f_\theta(x_k)] = \mathbb{E}[\nabla_{h_k^{L-1}} g_L(h_k^{L-1}) \dots \nabla_{x_k} g_1(x_k)], \quad (17)$$

which is also analytically intractable. We facilitate computation by making the assumption that the mutual information between nonlinear feature maps of different layers is small

$$\int p(h_k^l, h_k^{l'}) \log \left\{ \frac{p(h_k^l, h_k^{l'})}{p(h_k^l)p(h_k^{l'})} \right\} dh_k^l dh_k^{l'} \approx 0, \quad (18)$$

for all pairs (l, l') with $l \neq l'$. Applying this assumption of decoupled activation maps on Eq. 17, we get

$$\mathbb{E}[\nabla_{x_k} f_\theta(x_k)] \approx \prod_{l=0}^{L-1} \mathbb{E}_{h_k^l}[\nabla_{h_k^l} g_{l+1}(h_k^l)]. \quad (19)$$

We test this assumption empirically by feeding a random input $x \sim N(0, I)$ into a neural net with two fully-connected and equally wide hidden layers. As depicted in Fig. 2, the nonlinear activation maps of different layers carry ignorable mutual information even for narrow architectures, e.g. 16 neurons. More interestingly, mutual information shrinks fast when the hidden layers get wider and get ignorably small for widths relevant for practical use, such as 64 neurons.

Now the problem reduces to taking the expectations of the individual gradient terms. Despite being intractable, these

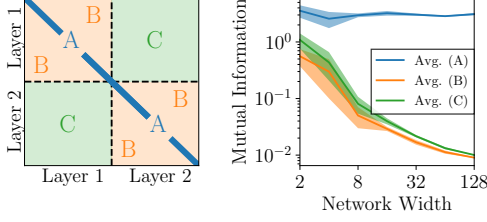


Figure 2. Nonlinear activations get statistically independent as the network width increases, supporting our assumption in Eq. 19. Imagine a matrix containing mutual information between all pairs of nonlinear activations h_k^l in a two-hidden-layer neural net as in the left panel. Group its entries into blocks: the diagonal block (A) giving the entropy of an activation, the within-layer off-diagonal block (B) giving the dependence of sibling activations, the cross-layer off-diagonal (C) giving the dependence of activations in different layers. As seen in the right panel, the average mutual information in blocks (B) and (C) decreases sharply with increasing layer width. Solid lines and shaded area represent average mutual information and its standard deviation over 100 repetitions.

expectations can be efficiently approximated by reusing the outcomes of the VMM step in Eq. 14 as follows

$$\begin{aligned} \mathbb{E}[\nabla_{h_k^l} g_{l+1}(h_k^l)] &\approx \mathbb{E}_{\tilde{h}_k^l}[\nabla_{\tilde{h}_k^l} g_{l+1}(\tilde{h}_k^l)] \\ &= \int \nabla_{\tilde{h}_k^l} g_{l+1}(\tilde{h}_k^l) \mathcal{N}(\tilde{h}_k^l | a_k^l, B_k^l) d\tilde{h}_k^l. \end{aligned} \quad (20)$$

We attain a deterministic approximation to Stein’s lemma by taking the covariance Σ_k from VMM and the expected gradient from Eq. 20:

$$\text{Cov}[x_k, f_\theta(x_k)] \approx \Sigma_k \prod_{l=0}^{L-1} \mathbb{E}_{\tilde{h}_k^l}[\nabla_{\tilde{h}_k^l} g_{l+1}(\tilde{h}_k^l)] := C_k. \quad (21)$$

We provide the expected gradient $[\nabla_{\tilde{h}_k^l} g_{l+1}(\tilde{h}_k^l)]$ for commonly used layer types in Sec. 3.5.

3.4. The Bidirectional Moment Matching Algorithm

Given an observed time series \tilde{X} , our deterministic method approximates the likelihood of a sequence as below:

$$p_{\theta, \phi}(X = \tilde{X}) \approx p(x_0 := \tilde{x}_0) \prod_{k=1}^K \mathcal{N}(x_k := \tilde{x}_k | \mu_k, \Sigma_k). \quad (22)$$

In the above expression, the moments of the normal density at each time step are calculated via HMM applying the below moment matching rules in time direction:

$$\begin{aligned} \mu_{k+1} &:= \mu_k + a_k^L \Delta t, \\ \Sigma_{k+1} &:= \Sigma_k + B_k^L \Delta t^2 + (C_k + C_k^T) \Delta t + D_k \Delta t, \end{aligned} \quad (23)$$

where $a_k^L \approx \mathbb{E}[f_\theta(x_k)]$, $B_k^L \approx \text{Cov}[f_\theta(x_k)]$, and $D_k \approx \mathbb{E}[L_\phi(x_k) L_\phi^T(x_k)]$ are obtained from VMM. The term

$C_k \approx \text{Cov}[x_k, f_\theta(x_k)]$ is obtained via Stein’s lemma. We refer to our method as *Bidirectional Moment Matching (BMM)* and provide its pseudocode in Algorithm 1.

Algorithm 1 Bidirectional Moment Matching (BMM)

Inputs: $f_\theta(\cdot) := g_L(g_{L-1}(\dots g_2(g_1(\cdot)) \dots))$ \triangleright Drift Net
 $L_\phi(\cdot) := u_L(u_{L-1}(\dots u_2(u_1(\cdot)) \dots))$ \triangleright Diffusion Net
 $\tilde{X} = \{\tilde{x}_0, \dots, \tilde{x}_K\}$ \triangleright Sequence
 $\mathcal{N}(\mu_0, \Sigma_0)$ \triangleright Initial distribution

Outputs: Likelihood $p_{\theta, \phi}(\tilde{X})$

for time step $k \in \{0, \dots, K-1\}$ **do** \triangleright Horizontal Moment Matching
 $\tilde{h}_k^0 \leftarrow \mathcal{N}(\mu_k, \Sigma_k)$ \triangleright Input distribution to drift and diffusion net
for layer index $l \in \{1, \dots, L\}$ **do** \triangleright Vertical Moment Matching
 See Sec. 3.5 for expectation, covariance, and Jacobian of g_l and u_l
 $a_k^l \leftarrow \mathbb{E}[g_l(\tilde{h}_k^{l-1})]$ \triangleright Drift net, expectation at layer l
 $B_k^l \leftarrow \text{Cov}[g_l(\tilde{h}_k^{l-1})]$ \triangleright Drift net, covariance at layer l
 $\tilde{h}_k^l \leftarrow \mathcal{N}(a_k^l, B_k^l)$ \triangleright Drift net, output distribution at layer l
 $J_k^l \leftarrow \mathbb{E}[\nabla_{\tilde{h}_k^{l-1}} g_l(\tilde{h}_k^{l-1})]$ \triangleright Drift net, Jacobian at layer l
 $c_k^l \leftarrow \mathbb{E}[u_l(\tilde{h}_k^{l-1})]$ \triangleright Diffusion net, expectation at layer l
 $D_k^l \leftarrow \text{Cov}[u_l(\tilde{h}_k^{l-1})]$ \triangleright Diffusion net, covariance at layer l
 $\tilde{v}_k^l \leftarrow \mathcal{N}(c_k^l, D_k^l)$ \triangleright Diffusion net, output distribution at layer l
end for
 $D_k \leftarrow (D_k^L + (c_k^L)(c_k^L)^T) \odot I$ \triangleright Diffusion net, second central moment
 $C_k \leftarrow \Sigma_k \prod_{l=1}^L J_k^l$ \triangleright Stein’s lemma
 $\mu_{k+1} \leftarrow \mu_k + a_k^L \Delta t$ \triangleright Mean and covariance at time step $k+1$
 $\Sigma_{k+1} \leftarrow \Sigma_k + B_k^L \Delta t^2 + (C_k + C_k^T) \Delta t + D_k \Delta t$
 $p_{\theta, \phi}(\tilde{x}_{k+1}) \leftarrow \mathcal{N}(\tilde{x}_{k+1} | \mu_{k+1}, \Sigma_{k+1})$ \triangleright Likelihood at time step $k+1$
end for
 $p_{\theta, \phi}(\tilde{X}) \leftarrow \mathcal{N}(\tilde{x}_0 | \mu_0, \Sigma_0) \prod_{k=1}^K p_{\theta, \phi}(\tilde{x}_{k+1})$ \triangleright Likelihood of sequence
return $p_{\theta, \phi}(\tilde{X})$

3.5. Moments of layers and their derivatives

Given the VMM output of the previous layer as $\tilde{h}_k^l \sim \mathcal{N}(a_k^l, B_k^l)$, we show below how these expressions can be calculated for three common layer types: (i) linear activations, (ii) nonlinear activations, and (iii) dropout.

Linear activations. The moments of an affine transformation $g_{l+1}(\tilde{h}_k^l) = W^{l+1} \tilde{h}_k^l + b^{l+1}$ are tractable as

$$\begin{aligned} \mathbb{E}[g_{l+1}(\tilde{h}_k^l)] &= W^{l+1} a_k^l + b^{l+1}, \\ \text{Cov}[g_{l+1}(\tilde{h}_k^l)] &= W^{l+1} B_k^l (W^{l+1})^T, \end{aligned} \quad (24)$$

where W^{l+1} and b^{l+1} correspond to the weights and bias of layer $l+1$. The expected gradient is then a constant

$$\mathbb{E}[\nabla_{\tilde{h}_k^l} g_{l+1}(\tilde{h}_k^l)] = W^{l+1}. \quad (25)$$

Nonlinear activations. The output moments of nonlinear activations are analytically not tractable. However, for many types of nonlinearities in widespread use, there exist tight approximations. For instance, the ReLU moments can be approximated as (Wu et al., 2019)

$$\begin{aligned} \mathbb{E}[\max(0, \tilde{h}_k^l)] &\approx \sqrt{\text{diag}(B_k^l)} SR \left(a_k^l / \sqrt{\text{diag}(B_k^l)} \right), \\ \text{Cov}[\max(0, \tilde{h}_k^l)] &\approx \sqrt{\text{diag}(B_k^l)} (B_k^l)^T F(a_k^l, B_k^l), \end{aligned} \quad (26)$$

where $\text{SR}(x) = \phi(x) + x\Phi(x)$ with ϕ and Φ representing the PDF and CDF of a standard Gaussian variable. We detail the function F in Appx. B. Since activation functions are applied element-wise, off-diagonal entries of the expected gradient are zero. The diagonal of the Jacobian of the ReLU function is the Heaviside step function (Wu et al., 2019)

$$\text{diag} \left(\mathbb{E} \left[\nabla_{\tilde{h}_k^l} g_{l+1}(\tilde{h}_k^l) \right] \right) \approx \Phi \left(a_k^l / \sqrt{\text{diag}(B_k^l)} \right). \quad (27)$$

Dropout. Define the dropout layer as the mapping $g_{l+1}(\tilde{h}_k^l) := \tilde{h}_k^l \odot z_k^l / q$ for a random vector z_k^l consisting of $\text{Bernoulli}(q)$ distributed entries. The moments of $g_{l+1}(\tilde{h}_k^l)$ are available as

$$\mathbb{E}[g_{l+1}(\tilde{h}_k^l)] = a_k^l, \quad (28)$$

$$\text{Cov}[g_{l+1}(\tilde{h}_k^l)] = B_k^l + \text{diag} \left(\frac{1-q}{q} (B_k^l + (a_k^l)(a_k^l)^T) \right).$$

See Appx. C for the details. Dropout is compatible to Stein’s lemma by re-interpreting $f_\theta(x_k)$ as a deterministic map of input and dropout noise variables $y_k = \{x_k, z_k^1, \dots, z_k^L\}$. The cross-covariance between x_k and $f_\theta(y_k)$ then reads

$$\begin{aligned} \text{Cov}[x_k, f_\theta(y_k)] &= \text{Cov}(x_k, y_k) \mathbb{E} [\nabla_{y_k} f_\theta(y_k)] \\ &= \Sigma_k \mathbb{E} [\nabla_{x_k} f_\theta(y_k)], \end{aligned} \quad (29)$$

since the covariance between x_k and z_k^l is zero. The Jacobian of the dropout layer is the identity matrix:

$$\mathbb{E} \left[\nabla_{\tilde{h}_k^l} g_{l+1}(\tilde{h}_k^l) \right] = \mathbb{E} [I z_k^l / q] = I. \quad (30)$$

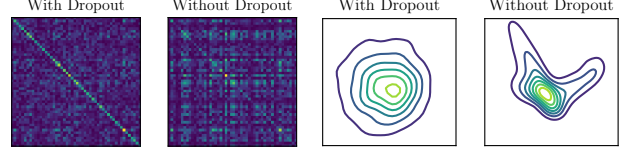
Dropout is useful to make VMM a tighter approximation. We demonstrate in Fig. 3a that dropout is helpful to decorrelate the co-variables of a layer, making their sum approach the normal distribution due to the *Central Limit Theorem* (CLT). We find it mild to assume a neural net layer to be wider than 20 neurons, which is sufficient for CLT to give an accurate approximation for practical purposes.

4. Experiments

We provide first an empirical investigation of our algorithm, and then benchmark against recent stochastic time series approaches in one standard synthetic environment with non-linear dynamics and two real-world forecasting applications.

4.1. Numerical properties

We investigate the numerical properties of the BMM algorithm in terms of integration error, computation cost, and generalization to multiple modes. We also compare cubature as an alternative choice to VMM, which is a standard numerical method for approximating the expectation of a smooth function with respect to a multivariate normal distribution. See Appx. D for details. We find out that VMM has favorable computational properties over cubature.



(a) Intermediate Activation. (b) Output Distribution.

Figure 3. Dropout decorrelates the activation map. We pass a multivariate normal distributed random vector through a neural net with three 50-neuron-wide hidden layers with ReLU activation. The off-diagonals of the covariance matrix of the activation map are suppressed when dropout is used after each ReLU activation, as shown in Panel (a) for an intermediate layer and Panel (b) for the output layer. Decorrelation of a large number of co-variables makes a normal distribution an accurate approximation on their sum due to the central limit theorem.

Approximation Error. In Fig. 4a, we evaluate how accurately VMM and cubature are able to approximate $\mathbb{E}[f_\theta(x)]$ for a normal input x and how approximation error is affected by neural net width and input/output dimensionality. For low dimensionalities, the relative error of VMM is approximately equal to cubature. The approximation error of VMM shrinks with increasing hidden layer width and dimensionality. This is expected since summing a larger number of decorrelated variables makes the assumption of normally distributed intermediate activations more accurate due to the central limit theorem (Wang & Manning, 2013).

Computational Cost. Propagation of S particles with dimensionality D along K time steps requires $\mathcal{O}(SKH^2)$ compute, when dynamics is governed by a NSDE with hidden layer width $H \geq D$. The computational cost of the NSDE is governed by the cost of the $H \times H$ -dimensional transformation in the hidden layer, which requires $\mathcal{O}(H^2)$ compute. Our method BMM approximates the $S \rightarrow \infty$ limit, while requiring only $\mathcal{O}(KH^3)$ compute. The additional factor H arises due to the approximation cost of the quadratic covariance. Replacing VMM with cubature in our framework results in an algorithm requiring $\mathcal{O}(KDH^2 + KD^3)$ compute. Cubature requires at least $\mathcal{O}(D)$ NSDE evaluations, which causes the additional factor D in the first term. The second term arises from the Cholesky decomposition of the input. We visualize in Fig. 4b the wall clock of VMM and cubature as a function of dimensionality and hidden layer width. Dimensionality sets a bottleneck for cubature, while it barely affects VMM. Contrarily, VMM gets significantly slower as the hidden layer width increases, while the computational cost of cubature remains similar. VMM is adaptable to setups requiring high learning capacity by building narrow and deep architectures. However, dimensionality of the time series signal is an external factor that limits the applicability of cubature.

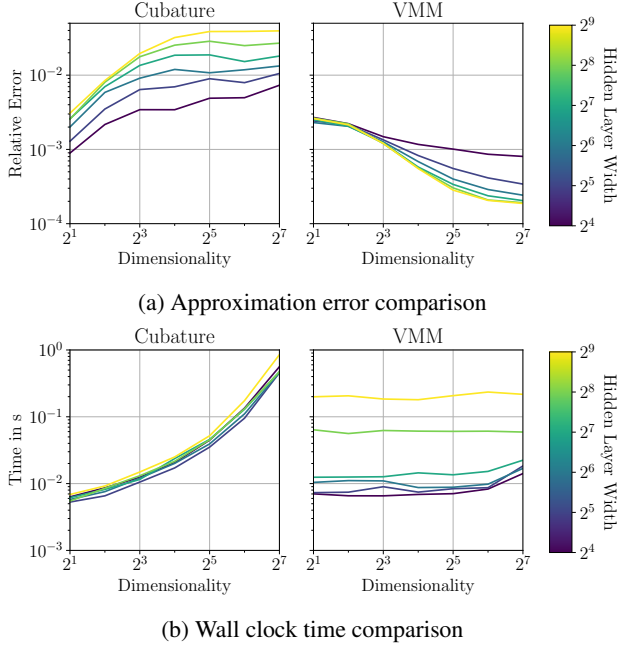


Figure 4. Comparison of VMM versus cubature in terms of approximation error and computation time. We generate a randomly initialized neural net $f_\theta(x)$. The dimensionalities of x and $f_\theta(x)$ are equal and vary in the horizontal axis of all plots. The neural net $f_\theta(x)$ has three fully-connected layers of varying widths color-coded according to the heatmap on the right of the figures, ReLU activation, and dropout with rate 0.2. As cubature cannot handle a random $f_\theta(x_k)$ and discontinuous activations, we evaluate it with tanh activation and without dropout. We aim to approximate the intractable expectation $r = \int f_\theta(x) \mathcal{N}(x|\tilde{\mu}, \tilde{\Sigma}) dx$, where $\tilde{\mu} \sim \mathcal{N}(0, I)$ and $\tilde{\Sigma} \sim \mathcal{W}(I, \dim(I))$ with Wishart distribution \mathcal{W} . We repeat the experiment 512 times and report the average relative error $\|r - \hat{r}\|^2 / \|r\|^2$ in Panel (a), where r is represented by averaging over 10 million Monte Carlo simulations and \hat{r} is approximated via cubature and VMM, respectively. We calculate the computation time of this experiment in all repetitions and report its average as a function of input dimensionality in Panel (b).

Multimodal Processes. Deterministic prediction of unimodal densities with NSDEs is an unsolved problem of its own. We restrict our focus on unimodal solutions, as the first inevitable step towards multimodal solutions. That being said, our method can generalize to multiple modes under mild assumptions. For instance, if training sequences come with the ground-truth knowledge of the modality they belong to, a separate unimodal NSDE can be fit to each mode and their mixture can be used during prediction. If modality assignments are not known a-priori, an initial clustering step can be applied. We visualize prediction results in Fig. 5 on the bimodal double-well dynamics, after clustering the training data and training a separate NSDE on each mode. In cases calling for more advanced solutions, BMM can serve as a subroutine in a Bayesian model, such as deterministic

variational inference of a Dirichlet process mixture model (Nieto-Barajas & Contreras-Cristan, 2014) or as part of a deep ensemble (Lakshminarayanan et al., 2017).

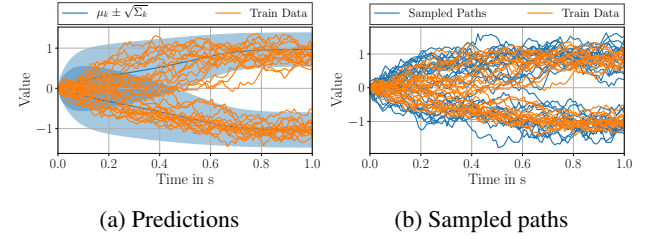


Figure 5. Handling multimodality with a NSDE applied to double-well potential dynamics: $dx_t = 4x_t(1 - x_t^2)dt + dw_t$. We train a separate model on each mode and predict with BMM in Panel (a), and with NSDE-MC in Panel (b).

4.2. Benchmarks

We benchmark on three different time series prediction datasets that enable a comparison to the state of the art methods for learning-based modeling of stochastics.

Datasets. We evaluate BMM on three data sets: (i) The stochastic Lotka-Volterra dynamics as a standard benchmark for modeling nonlinear systems, serving as a controlled setup with available ground truth model, (ii) The Beijing air quality dataset (Zhang et al., 2017) containing a high-dimensional sequence of hourly measurements of particle concentrations, temperature, and other features at three different locations in the city, (iii) The 3-DOF-Robot dataset (Agudelo-España et al., 2020) consisting of measurements on a three degree-of-freedom torque controlled real robot arm, which was recorded at two separate operating modes, low frequency (IID) and high frequency (Transfer). We give full experimental details in Appx. E.

Baselines. We benchmark our method (BMM) against: (i) *NODE* (Chen et al., 2018): Neural ODE, hence NSDE without diffusion, (ii) *NSDE-MC* (Tzen & Raginsky, 2019; Li et al., 2020): Monte Carlo sampling-based prediction with NSDE, (iii) *diffWGP* (Jorgensen et al., 2020): A SDE with drift and diffusion modeled as the predictive mean and covariance of a sparse GP, the state of the art of differential equation modeling with GPs, (iv) *Cubature*: A variant of ours using cubature in place of VMM to approximate μ_{k+1} in Eq. 12 and covariance Σ_{k+1} in Eq. 13.

Evaluation Criteria. We evaluate BMM against the baselines with respect to prediction accuracy by *Mean Squared Error (MSE)* and uncertainty calibration by *Negative Log-Likelihood (NLL)* and *Expectation of Coverage Probability Error (ECPE)* (Cui et al., 2020). ECPE measures the calibration of a model as the absolute difference between the

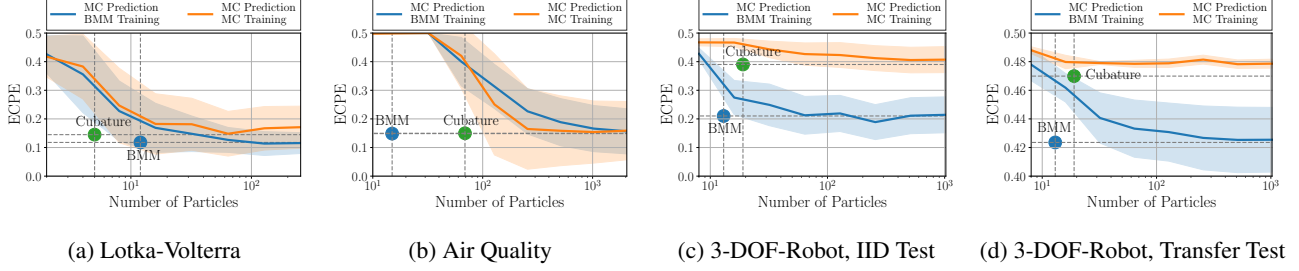


Figure 6. Cost-benefit analysis of calibration with different methods. One particle is equal to one Monte Carlo simulation along a trajectory. BMM is our proposed method, Cubature is our method with cubature as a replacement for VMM, the orange line is training and prediction with Monte Carlo sampling, and the blue line is training with our method and prediction with Monte Carlo sampling. In all four data sets, the minimum calibration error is achieved with low computational cost if our deterministic method is used for both training and prediction. We show mean and standard deviation over 10 runs.

Table 1. Forecasting results for: (i) Lotka-Volterra (2 dimensions, 100 time steps), (ii) Air Quality (34 dimensions, 47 time steps), and (iii) 3-DOF-Robot (9 output dimensions, 3 input dimensions, 100 time steps). We provide average and standard error over 10 runs.

Model	Lotka-Volterra		Air Quality		3-DOF-Robot				
	MSE	NLL	MSE	NLL	IID		Transfer		
NODE (Chen et al., 2018)	1.98 ± 0.04	-	1.85 ± 0.15	-	0.22 ± 0.01	-	29.78 ± 1.66	-	-
diffWGP (Jorgensen et al., 2020)	-	-	2.39 ± 0.04	$46.92^1 \pm 0.75$	-	-	-	-	-
NSDE-MC (Tzen & Raginsky, 2019)	2.07 ± 0.11	4.95 ± 0.44	1.90 ± 0.07	43.84 ± 0.75	0.22 ± 0.02	21.69 ± 1.75	30.52 ± 1.97	1821 ± 12	-
NSDE-Cubature (Ours, Ablation)	1.91 ± 0.08	4.84 ± 0.19	1.45 ± 0.04	37.84 ± 0.39	0.22 ± 0.02	5.65 ± 0.33	31.32 ± 1.89	352 ± 27	-
NSDE-BMM (Ours, Proposed)	1.75 ± 0.03	4.35 ± 0.15	1.44 ± 0.10	34.38 ± 0.50	0.16 ± 0.01	7.27 ± 1.31	12.31 ± 1.16	102 ± 12	-

true and predicted frequency of data in a specified interval. Loosely speaking, ECPE is small if p percent of the data lies in the predicted p -percent confidence interval. We provide further details on ECPE and our extension to the multivariate case in Appx. F.

Results. As shown in Tab. 1, BMM outperforms all base-lines in all data sets with respect to both NLL and MSE, with the only exception of NLL in the 3-DOF-Robot (IID) data set where it comes behind Cubature. We attribute the improved prediction accuracy of BMM over cubature to its reduced approximation error, as demonstrated in Fig. 4a. BMM proves to make more accurate predictions than both NSDE-MC and diffWGP probably due to the improved stability of the training process thanks to its deterministic objective. This outcome is despite the fact that diffWGP models the diffusion as a Wishart process, while BMM uses a diagonal diffusion function.

We present Fig. 6 as our main result: *The BMM algorithm reaches a level of uncertainty calibration, which is prohibitively costly for MC sampling.* In all three applications, MC sampling requires more than 50 roll-outs on the full sequence to match the ECPE, which our deterministic BMM

provides. BMM is separately applicable at training and prediction times. We find out that BMM improves on MC sampling in the 3-DOF-Robot data set even when used only for training, as visible from the blue curves in Fig. 6c and 6d being much steeper than the orange curves. We skip the MC training and BMM prediction variant, as it is already represented by the right extreme of the orange curves. We observe BMM to bring smaller ECPE than cubature in three of the four plots at comparable computational cost.

5. Conclusion

NSDEs have high expressive power due to the neural nets that govern drift and diffusion. This advantage comes at the expense of challenging computational characteristics that cause artifacts in uncertainty quantification, endangering their use in safety-critical applications. We demonstrate how a novel adaptation of moment matching approaches to NSDEs can give access to high quality prediction uncertainties much more affordably than black-box MC sampling. We also report deterministic NSDE training to improve prediction accuracy.

Despite being computationally efficient at large, introducing low-rank approximations on the covariance calculation such as $\Sigma_k \approx \text{diag}(u_k) + v_k v_k^T$ could speed up BMM further. Generalization of our findings to control and model-based reinforcement learning is also a topic for future work.

¹After correspondence with the Authors we present in this paper the correct NLL for diffWGP (Jorgensen et al., 2020). In the original paper an unknown issue caused a shift of the NLL.

References

- Abbati, G., Wenk, P., Osborne, M., Krause, A., Schölkopf, B., and Bauer, S. AReS and MaRS Adversarial and MMD-Minimizing Regression for SDEs. In *ICML*. 2019.
- Agudelo-España, D., Zadaianchuk, A., Wenk, P., Garg, A., Akpo, J., Grimminger, F., Viereck, J., Naveau, M., Righetti, L., Martius, G., Krause, A., Schölkopf, B., Bauer, S., and Wüthrich, M. A Real-Robot Dataset for Assessing Transferability of Learned Dynamics Models. In *ICRA*. 2020.
- Bensimhou, M. N-Dimensional cumulative function, and other useful facts about Gaussians and normal densities. 2013.
- Chen, T. Q., Rubanova, Y., Bettencourt, J., and Duvenaud, D. K. Neural Ordinary Differential Equations. In *NeurIPS*. 2018.
- Cui, P., Hu, W., and Zhu, J. Calibrated Reliable Regression using Maximum Mean Discrepancy. In *NeurIPS*. 2020.
- Ghosh, S., Fave, F., Delle, M., and Yedidia, J. Assumed Density Filtering Methods for Learning Bayesian Neural Networks. In *AAAI*. 2016.
- Haussmann, M., Gerwin, S., and Kandemir, M. Bayesian Evidential Deep Learning with PAC Regularization, 2020.
- Hegde, P., Heinonen, M., Lähdesmäki, H., and Kaski, S. Deep learning with differential Gaussian process flows. In *AISTATS*. 2019.
- Hernandez-Lobato, J. M. and Adams, R. Probabilistic Back-propagation for Scalable Learning of Bayesian Neural Networks. In *ICML*. 2015.
- Jorgensen, M., Deisenroth, M. P., and Salimbeni, H. Stochastic Differential Equations with Variational Wishart Diffusions. In *ICML*. 2020.
- Kingma, D. P. and Ba, J. Adam: A Method for Stochastic Optimization. In *ICLR*. 2015.
- Kuleshov, V., Fenner, N., and Ermon, S. Accurate Uncertainties for Deep Learning Using Calibrated Regression. In *ICML*. 2018.
- Lakshminarayanan, B., Pritzel, A., and Blundell, C. Simple and Scalable Predictive Uncertainty Estimation using Deep Ensembles. In *NeurIPS*. 2017.
- Li, X., Wong, T. L., Chen, R. T. Q., and Duvenaud, D. Scalable Gradients for Stochastic Differential Equations. In *AISTATS*. 2020.
- Liu, J. S. Siegel’s formula via Stein’s identities. *Statistics & Probability Letters*, 21, 1994.
- Look, A. and Kandemir, M. Differential Bayesian Neural Networks. In *NeurIPS Workshop Bayesian Deep Learning*. 2019.
- Nieto-Barajas, L. E. and Contreras-Cristan, A. A Bayesian Nonparametric Approach for Time Series Clustering. *Bayesian Analysis*, 0, 2014.
- Oksendal, B. *Stochastic Differential Equations: An Introduction with Applications*. Springer, 1992.
- Platt, J. C. Probabilistic Outputs for Support Vector Machines and Comparisons to Regularized Likelihood Methods. In *Advances in Large Margin Classifiers*. 1999.
- Ryder, T., Golightly, A., McGough, A. S., and Prangle, D. Black-Box Variational Inference for Stochastic Differential Equations. In *ICML*. 2018.
- Särkkä, S. and Sarmavuori, J. Gaussian filtering and smoothing for continuous-discrete dynamic systems. *Signal Processing*, 93, 2013.
- Särkkä, S. and Solin, A. *Applied Stochastic Differential Equations*. Cambridge University Press., 2019.
- Thiagarajan, J. J., Venkatesh, B., Sattigeri, P., and Bremer, P. Building Calibrated Deep Models via Uncertainty Matching with Auxiliary Interval Predictors. In *AAAI*. 2020.
- Tzen, B. and Raginsky, M. Neural Stochastic Differential Equations: Deep Latent Gaussian Models in the Diffusion Limit. *ArXiv*, abs/1905.09883, 2019.
- Wan, E. A. and Merwe, R. V. D. The Unscented Kalman Filter for Nonlinear Estimation. 2000.
- Wang, S. and Manning, C. Fast dropout training. In *ICML*. 2013.
- Wu, A., Nowozin, S., Meeds, E., Turner, R. E., Hernandez-Lobato, J. M., and Gaunt, A. L. Deterministic Variational Inference for Robust Bayesian Neural Networks. In *ICLR*. 2019.
- Zhang, S., Bin, G., Anlan, D., Jing, H., Ziping, X., and Xi, C. S. Cautionary tales on air-quality improvement in Beijing. *Proceedings of the Royal Society: Mathematical, Physical and Engineering Sciences*, 473, 2017.

A. Derivation of Mean and Covariance for Horizontal Moment Matching

We approximate the marginal distribution at an arbitrary time step as $p_{\theta, \phi}^{\text{EM}}(x_{k+1}) \approx \mathcal{N}(x_{k+1} | \mu_{k+1}, \Sigma_{k+1})$. By reparameterizing $p_{\theta, \phi}^{\text{EM}}(x_{k+1})$ we obtain

$$\begin{aligned} z_k &\sim N(z_k | 0, I), & x_k &\sim \mathcal{N}(x_k | \mu_k, \Sigma_k), \\ x_{k+1} &:= x_k + f_\theta(x_k)\Delta t + L_\phi(x_k)\sqrt{\Delta t}z_k, \end{aligned}$$

where I is the identity matrix with the dimensionality appropriate for the context. Mean μ_{k+1} and covariance Σ_{k+1} at time step $k+1$ can be expressed as

$$\mu_{k+1} = \mu_k + \mathbb{E}[f_\theta(x_k)]\Delta t.$$

$$\Sigma_{k+1} = \Sigma_k + \text{Cov}[f_\theta(x_k)]\Delta t^2 + \text{Cov}[f_\theta(x_k), x_k]\Delta t + \text{Cov}[f_\theta(x_k), x_k]^T\Delta t + \mathbb{E}[L_\phi(x_k)L_\phi^T(x_k)]\Delta t,$$

where $\text{Cov}[f_\theta(x_k), x_k]$ denotes the cross-covariance between the random vectors in the arguments. In order to derive this result we hinge on (Särkkä & Solin, 2019) (pg. 174 Eq. 9.32 and 9.33), in which analytical solutions to SDEs by inserting a discretization scheme are proposed. Using the law of the unconscious statistician we obtain for the next mean

$$\mu_{k+1} = \mathbb{E}[x_k + f_\theta(x_k)\Delta t + L_\phi(x_k)\sqrt{\Delta t}z_k] = \mu_k + \mathbb{E}[f_\theta(x_k)\Delta t] + \underbrace{\mathbb{E}[L_\phi(x_k)\sqrt{\Delta t}z_k]}_{=0} = \mu_k + \mathbb{E}[f_\theta(x_k)\Delta t].$$

In order to derive a tractable expression for the next covariance $\Sigma_{k+1} = \mathbb{E}[x_{k+1}x_{k+1}^T] - \mathbb{E}[x_{k+1}]\mathbb{E}[x_{k+1}]^T$ we first evaluate the expectation $\mathbb{E}[x_{k+1}x_{k+1}^T]$

$$\begin{aligned} \mathbb{E}[x_{k+1}x_{k+1}^T] &= \mathbb{E}[(x_k)(x_k)^T + (x_k)(f_\theta(x_k)\Delta t)^T + (x_k)(L_\phi(x_k)\sqrt{\Delta t}z_k)^T + \\ &\quad (f_\theta(x_k)\Delta t)(x_k)^T + (f_\theta(x_k)\Delta t)(f_\theta(x_k)\Delta t)^T + (f_\theta(x_k)\Delta t)(L_\phi(x_k)\sqrt{\Delta t}z_k)^T + \\ &\quad (L_\phi(x_k)\sqrt{\Delta t}z_k)(x_k)^T + (L_\phi(x_k)\sqrt{\Delta t}z_k)(f_\theta(x_k)\Delta t)^T + (L_\phi(x_k)\sqrt{\Delta t}z_k)(L_\phi(x_k)\sqrt{\Delta t}z_k)^T] \\ &= \mathbb{E}[(x_k + f_\theta(x_k)\Delta t)(x_k + f_\theta(x_k)\Delta t)^T] + \mathbb{E}[(L_\phi(x_k))(L_\phi(x_k))^T]\Delta t, \end{aligned}$$

since $\mathbb{E}[z_k] = 0$ and $\mathbb{E}[z_k z_k^T] = I$. Using the bilinearity of the covariance operator we obtain

$$\begin{aligned} \Sigma_{k+1} &= \mathbb{E}[(x_k + f_\theta(x_k)\Delta t)(x_k + f_\theta(x_k)\Delta t)^T] - \mathbb{E}[(x_k + f_\theta(x_k)\Delta t)]\mathbb{E}[(x_k + f_\theta(x_k)\Delta t)]^T + \mathbb{E}[(L_\phi(x_k))(L_\phi(x_k))^T]\Delta t \\ &= \text{Cov}(x_k + f_\theta(x_k)\Delta t) + \mathbb{E}[L_\phi(x_k)L_\phi^T(x_k)]\Delta t \\ &= \text{Cov}(x_k) + \text{Cov}(x_k, f_\theta(x_k)\Delta t) + \text{Cov}(f_\theta(x_k)\Delta t, x_k) + \text{Cov}(f_\theta(x_k)\Delta t) + \mathbb{E}[L_\phi(x_k)L_\phi^T(x_k)]\Delta t. \end{aligned}$$

B. Moments of ReLU Activation

The output moments of the ReLU activation $g_{l+1}(\tilde{h}_k^l) = \max(0, \tilde{h}_k^l)$, with $\tilde{h}_k^l \sim \mathcal{N}(a_k^l, B_k^l)$, function can be estimated as (Wu et al., 2019)

$$\begin{aligned} \mathbb{E}[g_{l+1}(\tilde{h}_k^l)] &= \sqrt{\text{diag}(B_k^l)} \text{SR} \left(a_k^l / \sqrt{\text{diag}(B_k^l)} \right), \\ \text{Cov}[g_{l+1}(\tilde{h}_k^l)] &= \sqrt{\text{diag}(B_k^l)} (B_k^l)^T F(a_k^l, B_k^l), \end{aligned}$$

with $F(a_k^l, B_k^l) = (A(a_k^l, B_k^l) + \exp -Q(a_k^l, B_k^l))$. We introduce the dimensionless variable $\epsilon_k^l = a_k^l / \sqrt{\text{diag}(B_k^l)}$ and obtain $\text{SR}(\epsilon_k^l) = (\phi(\epsilon_k^l) + \epsilon_k^l \Phi(\epsilon_k^l))$, with ϕ and Φ representing the standard normal PDF and CDF. We take $\sqrt{\cdot}$ elementwise in this expression. The matrix valued function $A(a_k^l, B_k^l)$ is estimated as

$$A(a_k^l, B_k^l) = \text{SR}(\epsilon_k^l) \text{SR}(\epsilon_k^l)^T + \rho_k^l \Phi(\epsilon_k^l) \Phi(\epsilon_k^l)^T, \quad (31)$$

with $\rho_k^l = B_k^l / \left(\sqrt{\text{diag}(B_k^l)} \sqrt{\text{diag}(B_k^l)^T} \right)$. The i, j -th element of $Q(a_k^l, B_k^l)$ can be estimated as:

$$Q(a_k^l, B_k^l)_{i,j} = -\log \left(\frac{g_{k_{i,j}}^l}{2\pi} \right) + \left(\frac{\rho_{k_{i,j}}^l}{2g_{k_{i,j}}^l (1 + \bar{\rho}_{k_{i,j}}^l)} \left((\epsilon_{k_i}^l)^2 + (\epsilon_{k_j}^l)^2 \right) - \frac{\arcsin(\rho_{k_{i,j}}^l) - \rho_{k_{i,j}}^l}{\rho_{k_{i,j}}^l g_{k_{i,j}}^l} \epsilon_{k_i}^l \epsilon_{k_j}^l \right) + \mathcal{O}((\epsilon_k^l)^4), \quad (32)$$

with $g_k^l = \arcsin(\rho_k^l) + \rho_k^l \odot (1 + \bar{\rho}_k^l)$, and $\bar{\rho}_k^l = \sqrt{1 - \rho_k^l \odot \rho_k^l}$. We denote with \odot elementwise division.

C. Moments of Dropout

Dropout can be viewed as a layer operating independently on each activation map as $g_{l+1}(\tilde{h}_k^l) := \tilde{h}_k^l \odot z_k^l / q$, where $z_k^l \sim \text{Bernoulli}(q)$ and $\tilde{h}_k^l \sim \mathcal{N}(a_k^l, B_k^l)$. The moments of which are available as

$$\begin{aligned} \mathbb{E}[g_{l+1}(\tilde{h}_k^l)] &= a_k^l, \\ \text{Cov}[g_{l+1}(\tilde{h}_k^l)] &= B_k^l + \text{diag} \left(\frac{1-q}{q} (B_k^l + (a_k^l)(a_k^l)^T) \right). \end{aligned} \quad (33)$$

In order to derive these expressions we omit for simplicity the rescaling by q . Using independence between \tilde{h}_k^l and z_k^l we obtain straightforwardly $\mathbb{E}[g_{l+1}(\tilde{h}_k^l)]$

$$\mathbb{E}[g_{l+1}(\tilde{h}_k^l)] = \mathbb{E}[\tilde{h}_k^l \odot z_k^l] = \mathbb{E}[\tilde{h}_k^l] \mathbb{E}[z_k^l] = q \mathbb{E}[a_k^l].$$

We derive diagonal and off-diagonal entries in $\text{Cov}[g_{l+1}(\tilde{h}_k^l)]$ separately. We obtain for $i = j$

$$\begin{aligned} \text{Cov}(g_{l+1}(\tilde{h}_k^l)_i, g_{l+1}(\tilde{h}_k^l)_i) &= \mathbb{E} \left[(g_{l+1}(\tilde{h}_k^l)_i)^2 \right] - \mathbb{E}[g_{l+1}(\tilde{h}_k^l)_i]^2 = \mathbb{E} \left[(\tilde{h}_{k_i}^l)^2 \right] \mathbb{E}[(z_{k_i}^l)^2] - q^2 \mathbb{E}[\tilde{h}_{k_i}^l]^2 \\ &= q \mathbb{E} \left[(\tilde{h}_{k_i}^l)^2 \right] - q^2 \mathbb{E}[\tilde{h}_{k_i}^l]^2 = q \text{Cov}(\tilde{h}_{k_i}^l, \tilde{h}_{k_i}^l) + q \mathbb{E}[\tilde{h}_{k_i}^l]^2 - q^2 \mathbb{E}[\tilde{h}_{k_i}^l]^2 \\ &= q \text{Cov}(\tilde{h}_{k_i}^l, \tilde{h}_{k_{k_i}}^l) + q(1-q) \mathbb{E}[\tilde{h}_{k_i}^l]^2 \end{aligned}$$

and for $i \neq j$

$$\begin{aligned} \text{Cov}(g_{l+1}(\tilde{h}_k^l)_i, g_{l+1}(\tilde{h}_k^l)_j) &= \mathbb{E} \left[g_{l+1}(\tilde{h}_k^l)_i g_{l+1}(\tilde{h}_k^l)_j \right] - \mathbb{E}[g_{l+1}(\tilde{h}_k^l)_i] \mathbb{E}[g_{l+1}(\tilde{h}_k^l)_j] = \mathbb{E} \left[\tilde{h}_{k_i}^l \tilde{h}_{k_j}^l z_{k_i}^l z_{k_j}^l \right] - q^2 \mathbb{E}[\tilde{h}_{k_i}^l] \mathbb{E}[\tilde{h}_{k_j}^l] \\ &= q^2 \mathbb{E} \left[\tilde{h}_{k_i}^l \tilde{h}_{k_j}^l \right] - q^2 \mathbb{E}[\tilde{h}_{k_i}^l] \mathbb{E}[\tilde{h}_{k_j}^l] = q^2 \text{Cov}(\tilde{h}_{k_i}^l, \tilde{h}_{k_j}^l). \end{aligned}$$

By vectorizing and rescaling with q we obtain the final expression.

D. Cubature

Cubature is a well known numerical integration method, which estimates the expected value of a nonlinear function $f(x_k)$ with respect to a Gaussian density $\mathcal{N}(x_k | \mu_k, \Sigma_k)$ as a weighted sum of point mass evaluations

$$\int f(x_k) \mathcal{N}(x_k | \mu_k, \Sigma_k) dx_k \approx \sum_{i=1}^C w_i f(\mu_k + \sqrt{\Sigma_k} \zeta_i), \quad (34)$$

where $\sqrt{\Sigma_k} \sqrt{\Sigma_k}^T = \Sigma_k$. The coefficients w_i and ζ_i are predetermined by a heuristic that aims to spread the particles around the support of the distribution in a maximally information preserving way. There exist multiple heuristics for choosing w_i and ζ_i . Such a heuristic is the *Unscented Transform* (UT), which is commonly used in the context of Kalman filtering (Wan & Merwe, 2000). UT can be formulated as a sum of $2D + 1$ elements for a D -dimensional input space as

$$w_i = \begin{cases} \frac{\lambda}{D+\kappa} & , i = 0, \\ \frac{1}{2(D+\kappa)} & , i = 1, \dots, 2D, \end{cases} \quad (35)$$

$$\zeta_i = \begin{cases} 0 & , i = 0, \\ \sqrt{\lambda + D}e_i & , i = 1, \dots, D, \\ -\sqrt{\lambda + D}e_{i-D} & , i = D + 1, \dots, 2D. \end{cases} \quad (36)$$

The constants λ and κ control the particle spread. The vectors e_i form the standard basis in D dimensions.

E. Experimental Details

NODE and NSDE models are trained on shorter snippets together with the Adam optimizer (Kingma & Ba, 2015) and its default hyperparameter settings. Given the observed state \hat{x}_0 , we chose the input distribution to our method (see Alg. 1) at the initial time step to be $\mathcal{N}(\hat{x}_0, I/10^6)$, which is an approximate delta distribution. Number of epochs and other method specific hyperparameters have been tuned manually for each method. We use a RK4 discretization for NODE and backpropagate directly through the solver.

Lotka-Volterra. We choose stochastic Lotka-Volterra equations as in (Abbati et al., 2019)

$$dx_t = \begin{bmatrix} 2x_{t,1} - x_{t,1}x_{t,2} \\ x_{t,1}x_{t,2} - 4x_{t,2} \end{bmatrix} dt + \sqrt{\begin{bmatrix} 0.05 & 0.03 \\ 0.03 & 0.09 \end{bmatrix}} dw_t.$$

We generate 128 paths using Euler-Maruyama discretization with a small step size of $dt = 10^{-5}$ seconds. Afterwards, we coarsen the data set such that 200 equally spaced observations between 0 – 10 seconds remain. First 100 observations are used for training and the remaining 100 observations for testing. We use a batch size of 16 and a prediction horizon of 10 for training.

Beijing Air Quality. The atmospheric air-quality data set from Beijing (Zhang et al., 2017) consists of hourly measures over the period 2014-2016 at three different locations. The air quality is characterized by 10 different features at each location. Including the timestamp we obtain in total 34 features. We follow (Jorgensen et al., 2020) for designing the experimental setup. The first two years of are used for training and we test on the first 48 hours in the year 2016. We use a batch size of 16 and a prediction horizon of 10 for training.

3-DOF-Robot. The 3-DOF-Robot dataset (Agudelo-España et al., 2020) consists of multiple trajectories with length 14000, 3 input and 9 output dimensions, recorded with a sampling rate of 1kHz. The dataset was recorded at two different operating modes: (i) 50 recordings of low frequency oscillations of the robot arm with a small moving range, and (ii) 50 recordings of high frequency oscillations with full moving range. We train on the first 38 trajectories and validate on the next 3 trajectories using the low frequency recordings. Test is performed on last 9 low frequency trajectories, denoted as IID, and last 9 high frequency recordings, denotes as Transfer. We use a batch size of 16 and a prediction horizon of 16 for training.

F. Expectation of Coverage Probability Error

The prediction quality is assessed in terms of *mean squared error* (MSE), *negative log-likelihood* (NLL), as well as the *expectation of coverage probability error* (ECPE). ECPE measures the absolute difference between true confidence and the empirical coverage probability as (Cui et al., 2020)

$$ECPE = \frac{1}{n} \sum_{n=1}^N |\hat{p}_j - p_j|, \quad (37)$$

where p_j and \hat{p}_j is the true frequency and empirical frequency, respectively. We choose 11 equally spaced confidence levels between 0 and 1. By taking the average over all test samples $x_k \in \mathcal{D}_{test}$, which lie in a predicted confidence interval, the empirical frequency is estimated as

$$\hat{p}_j = \frac{\sum_k^{|\mathcal{D}_{test}|} \mathbb{I}\{x_k \leq \hat{F}_k^{-1}(p_j)\}}{|\mathcal{D}_{test}|}. \quad (38)$$

In contrast to Cui et al. (2020), we consider in our work the case of multivariate predictors, which complicates the estimation of the predicted inverse cumulative distribution function \hat{F}_k^{-1} . However, if x_k is normally distributed, we can analytically

estimate \hat{F}_k^{-1} as a function of model outputs μ_k and Σ_k . As discussed by [Bensimhou \(2013\)](#), we may define the cumulative distribution function as the probability that a sample lies inside the ellipsoid determined by its Mahalanobis distance r . The ellipsoidal region is analytically obtained as

$$(x_k - \mu_k)^T \Sigma_k^{-1} (x_k - \mu_k) \leq \chi_D^2(p) = \hat{F}_k^{-1}(p), \quad (39)$$

where χ_D^2 is the chi-squared distribution with D degrees of freedom.

G. Network Architecture

For all experiments we use similar architectures as competing methods. For NSDEs with cubature we use the same architectures except exchanging ReLU with tanh.

Lotka-Volterra.



Figure 7. NSDE architecture for Lotka-Volterra experiment.

Beijing Air Quality.



Figure 8. NSDE architecture for Air quality experiment.

3-DOF-Robot.



Figure 9. NSDE architecture for 3-DOF-Robot experiment.